
FROM WINTER STORM THERMODYNAMICS TO WIND GUST EXTREMES: DISCOVERING INTERPRETABLE EQUATIONS FROM DATA

Frederick Iat-Hin Tam

Faculty of Geosciences and Environment
University of Lausanne
Lausanne, VD, Switzerland

Fabien Augsburger

Faculty of Geosciences and Environment
University of Lausanne
Lausanne, VD, Switzerland

Tom Beucler

Faculty of Geosciences and Environment
University of Lausanne
Lausanne, VD, Switzerland

April 11, 2025

ABSTRACT

Reliably identifying and understanding temporal precursors to extreme wind gusts is crucial for early warning and mitigation. This study proposes a simple data-driven approach to extract key predictors from a dataset of historical extreme European winter windstorms and derive simple equations linking these precursors to extreme gusts over land. A major challenge is the limited training data for extreme events, increasing the risk of model overfitting. Testing various mitigation strategies, we find that combining dimensionality reduction, careful cross-validation, feature selection, and a nonlinear transformation of maximum wind gusts informed by Generalized Extreme Value distributions successfully reduces overfitting. These measures yield interpretable equations that generalize across regions while maintaining satisfactory predictive skill. The discovered equations reveal the association between a steady drying low-troposphere before landfall and wind gust intensity in Northwestern Europe.

1 Introduction

Damaging windstorms associated with extratropical cyclones are among the leading weather-related disasters in the mid-latitudes winters, especially in Europe [Schwierz et al., 2010]. From a weather forecasting standpoint, early detection of reliable precursors leading to extreme windstorms helps timely disaster mitigation. Beyond horizontal temperature differences strengthening storms [Laurila et al., 2021], studies have highlighted how lower-atmosphere humidity fuels wind jets [Martínez-Alvarado et al., 2013] and transports high-wind air toward the surface [Browning et al., 2015], yet simple models linking winterstorm characteristics to wind gusts are lacking.

Interpretable machine learning has enabled trustworthy data-driven models of thunderstorms [Hilburn, 2023] and tropical cyclones [Tam et al., 2024], improving process understanding by reducing the attribution uncertainty of post-hoc explainable AI methods [Mamalakis et al., 2023]. This motivates us to apply data-driven methods to uncover novel temporal patterns in environmental precursors to extreme European windstorms. A key challenge is the limited availability of extreme storm data, which restricts the use of complex nonlinear models prone to overfitting in small-sample conditions. However, this limitation also presents an opportunity to derive a simple, interpretable equation approximating complex physical processes, paving the way for data-driven discovery.

Data-driven equation discovery distills simple laws from empirical data [Schmidt and Lipson, 2009] with methods ranging from sparse selection algorithms to symbolic regression [Song et al., 2024]. While data-driven approaches have

successfully identified physical laws from controlled fluid dynamics experiments data [Brunton et al., 2016, Cheng and Alkhalifah, 2024], finding interpretable equations from noisy, multidimensional weather and climate data remains under-explored. Balancing model performance and algorithmic complexity, [Grundner et al., 2024] uncovered simple analytical cloud cover equations from high-resolution model outputs. We similarly implement a hierarchical modeling framework to track the trade-off between the model complexity and generalization capability, identifying a set of sparse yet descriptive equations that achieves satisfactory prediction skills for unseen storm cases across European regions. Additionally, we explore the best strategy for dimensionality reduction and feature selection for reliable discovery of simple equations from small yet high-dimensional datasets.

2 Data

2.1 Raw Datasets Description

Winter Windstorm Tracks for Europe The winter storm data analyzed in this study is based on the ECMWF Winter Windstorm Indicator dataset [Copernicus Climate Change Service, Climate Data Store, 2022]. This dataset documents historical severe windstorms between 1979 and 2021, and their footprints. The tracking of storms is performed by applying a tracking algorithm on the ERA5 reanalysis data from October through March. The tracking algorithm tracks local maxima of 850 hPa relative vorticity, with a minimal 10m wind speed threshold of 25 m s^{-1} . A total of 118 storms is identified in the 42-year period. This study analyzes storms in the last 30 years (96 storms). Since we focus on the impact of severe windstorms over land in this study, short-lived or non-landfalling storms are filtered out, which leaves us with 63 storms.

ERA5 Meteorological Reanalysis We use the hourly ERA5 reanalysis dataset with a horizontal resolution of 0.25° - 0.25° to characterize the environmental conditions for all tracked storms. Our analysis considers 28 potential environmental drivers for wind gust formation and intensity [Schulz and Lerch, 2022] listed in Table SI6. To find the driver conditions local to each storm, we adopt a system-following 4° - 4° grid box centered around the storm track of all 28 environmental drivers. These drivers include measurements of the winterstorm kinematics (e.g., 10m wind speeds), precipitation characteristics (e.g., mean precipitation rates), and the thermodynamic characteristics (e.g., latent heat flux; K-index) near the windstorms. A full list of the ERA5 variables and their units is provided in Table S6.

2.2 Data Preprocessing: Dimensionality Reduction and Partitioning

Focusing on extreme events limits the training data for data-driven models. To ensure reliable equation discovery, we reduce the dimensionality of storm history and post-landfall gust data, turning our dataset into one that can be analyzed with simple data-driven models without overfitting.

Features: Prescribed Spatial Dimensionality Reduction To encode the 4D storm history fields as time series, we compute four spatial statistics: maximum (max), minimum (min), mean, and standard deviation (std). Using predefined statistics instead of learned filters facilitates physical interpretability. For example, a higher temperature standard deviation may indicate the presence of weather fronts [Lagerquist et al., 2022]. To further reduce dimensionality, we apply Principal Component Analysis (PCA) to compress time series into orthogonal temporal modes ($\Pi_X(t)$) and PC loadings (PC_X), which are scalars denoting the projection of time series onto $\Pi_X(t)$:

$$X(t) - \overline{X(t)} = \sum_{i=1}^N \text{PC}_{X,i} \Pi_{X,i}(t), \quad \text{where} \quad \langle \Pi_{X,i}(t) | X(t) \rangle_X = \text{PC}_{X,i}. \quad (1)$$

Here, N is the number of retained PC modes indexed by i , and $\langle \cdot | \cdot \rangle_X$ denotes the inner product associated with the PCA decomposition of X . The modes $\Pi_{X,i}(t)$ are normalized such that $\langle \Pi_{X,i}(t) | \Pi_{X,j}(t) \rangle_X = \delta_{ij}$ where δ_{ij} is the Kronecker delta, ensuring orthonormality of the PC modes.

Targets: Geographical Clustering In a low-sample-size regime, predicting wind gusts for every pixel across Europe is impractical and difficult to interpret. We use K-means++ clustering [Arthur and Vassilvitskii, 2006] to partition the landmass into K subregions, incorporating elevation, latitude, longitude, and maximum gusts from 63 severe windstorms. This ensures clusters reflect windstorm gust characteristics while remaining spatially coherent. To enforce geographical contiguity, we apply k-nearest neighbors [Enas and Choi, 1986], reassigning edge pixels based on the most frequent cluster label. Although silhouette scores suggest an optimal $K = 4$ - 5 (Fig. S1), these clusters group disjointed regions with distinct wind gust characteristics (Fig. S2). We therefore consider three additional clustering metrics (e.g., [Xie and Beni, 1991]), which identify local optima at $K = 9$, 14 , and 15 (Fig. S3). Among these, $K = 15$ best

preserves geographical compactness and aligns with established European climatic zones [Jylhä et al., 2010] (Fig. S4). With clusters defined, we extract, for each storm, the highest instantaneous 10m wind gust within each cluster during the 15 hours post-landfall. This window ensures short-lived but intense storms like Lothar [Wernli et al., 2002] are included. Our target is the maximum 15-hour wind gust within each cluster ($U_{\text{gust},i}$), where i indexes the 15 clusters.

Cross-Validation Procedure To ensure data-driven models select gust predictors applicable to severe windstorms, we always leave out the same 7 storms for testing. The test set is randomly chosen, except for the Lothar storm, which is explicitly withheld to assess performance on an extreme, unseen case. The remaining 56 storms are split into 7 training-validation folds by randomly selecting 7 sets of 8 storms without replacement for validation ("Random split"). Alternatively, as a step toward invariant causal prediction [Peters et al., 2016], we identify features robust to distributional shifts by clustering the output vector U_{gust} into 7 groups via K-means++ (Table S2). We then train on 6 clusters and validate on the remaining one, repeating this process 7 times ("ICP split"), following [Häfner et al., 2023]. [Sweet et al., 2023] shows that such an "ICP split" outperforms naive k-fold cross-validation for regression.

2.3 Extreme Value Theory for Wind Gust Distributions

Assessing wind gust severity relative to local climatology and distinguishing moderate from extreme gusts are key to risk assessment. We describe extreme gusts using the Generalized Extreme Value (GEV) distribution, a family of continuous distributions designed for block maxima such as extreme sea levels [Méndez et al., 2007]. The cumulative distribution function (CDF) and its functional inverse (quantile function) are

$$G_{\mu,\sigma,\xi}(x) = \begin{cases} \exp \left[- \left(1 + \xi \frac{x-\mu}{\sigma} \right)^{-\frac{1}{\xi}} \right], & \xi \neq 0, \\ \exp \left[- \exp \left(-\frac{x-\mu}{\sigma} \right) \right], & \xi = 0, \end{cases} \quad G_{\mu,\sigma,\xi}^{-1}(p) = \begin{cases} \mu + \frac{\sigma}{\xi} \left[(-\ln p)^{-\xi} - 1 \right], & \xi \neq 0, \\ \mu - \sigma \ln(-\ln p), & \xi = 0. \end{cases} \quad (2)$$

where $\mu \in \mathbb{R}$ (location), $\sigma \in \mathbb{R}_+^*$ (scale), and $\xi \in \mathbb{R}$ (shape). Unlike empirical CDFs, the GEV enables extrapolation beyond observed data to estimate return periods for extreme events. Due to the high spatial variability in land surface and topography across Europe, we fit a separate GEV for each cluster (Fig. 1c-e; Table S1). After testing multiple definitions and durations for block maxima sampling, we opted for *daily* maximum gusts over all cluster grid points during winter months (Fig. S5). This approach differentiates regions frequently impacted by strong gusts from those less affected (Fig. 1a,d) and allows modeling of unseen extremes, which empirical distributions cannot capture (Fig. 1b).

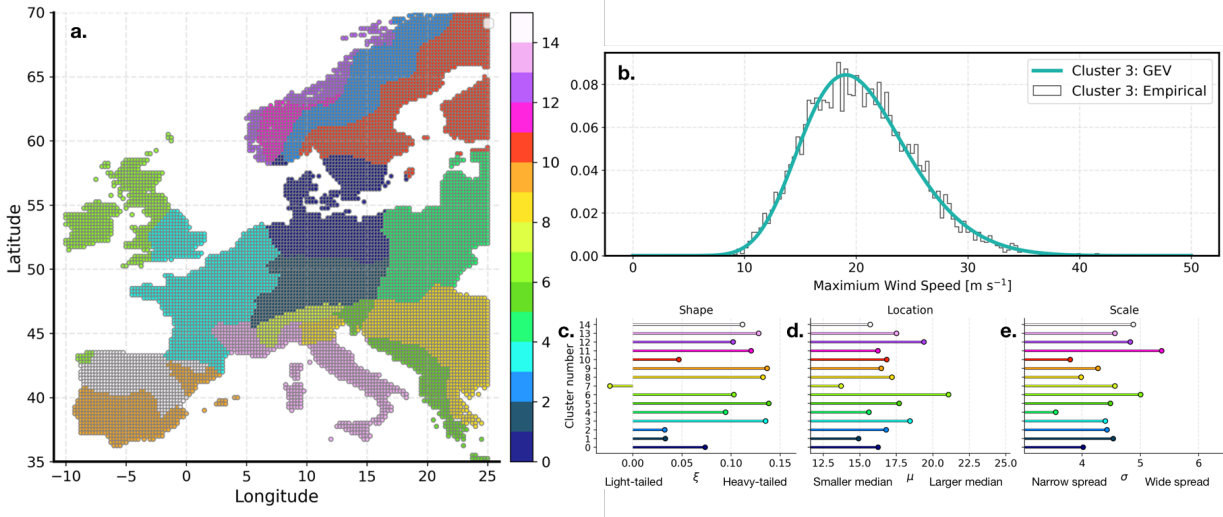


Figure 1: (a) We derive geographically contiguous regions of the European continent via K-means++ and kNN clustering to define maximum wind gust targets. (b) Extreme gust distributions are modeled using the GEV distribution, with shape (c), location (d), and scale (e) parameters fitted for each region.

3 Methodology

Feature Selection We aim to derive *interpretable* equations linking storm characteristics to post-landfall gusts. Even with prescribed spatial statistics and PCA for dimensionality reduction, the number of features (28 predictors \times 4 spatial

statistics \times 1–12 PC loadings) still far exceeds the number of training and validation samples (56). To address this underdetermined problem, we apply sequential forward feature selection, minimizing the mean or maximum validation root-mean-squared error (RMSE) across our 7 cross-validation splits. Features are added until the RMSE objective no longer decreases.

Model Hierarchy We construct a hierarchy of data-driven models expressible as simple equations by training multiple linear regressions (MLR) with PC loadings as features while varying three hyperparameters: feature smoothing, retained feature variance, and target transformation. For feature smoothing, we apply a low-pass rectangular filter to the PC loading time series, testing cutoff frequencies from 0.52 rad/hr to 1.92 rad/hr. For retained variance, we set four thresholds to determine the number of retained PC components per predictor: [75%, 80%, 85%, 90%]. The number of retained PC components per predictor acts as a regularization hyperparameter controlling the predictor variance fed to the ML framework. Finally, we explore a nonlinear, data-adaptive transformation of maximum wind gusts to encourage out-of-distribution generalization for extremes [Buriticá and Engelke, 2024]. For each sample, we first obtain its percentile value from the CDF fitted in each region, then apply a nonlinear transformation to better distinguish extreme values in the GEV distribution tails: $Z_i = -\ln[1 - \text{CDF}_i(U_{\text{gust},i})]$, where Z is the transformed target, and CDF_i is the cumulative distribution function of the GEV fitted in region i . All MLRs are trained using the least squares algorithms from the Scikit-Learn Python package [Pedregosa et al., 2011].

Pareto Optimality for Equation Discovery Balancing performance and complexity is a multi-objective optimization task that can be addressed through Pareto optimization [Jin and Sendhoff, 2008]. Following sequential feature selection, we select optimal models from the empirical ‘‘Pareto front’’, corresponding to the lowest error achieved for a given complexity before the mean (or max) validation RMSE across 7 cross-validation splits plateaus. We define complexity as the number of unique features (predictor + spatial statistic) selected, as this better reflects equation simplicity than, for instance, the number of trainable parameters.

Model Evaluation Pareto optimization seeks models with the lowest error while maintaining simplicity. We evaluate model performance using the mean validation RMSE across 7 folds and measure complexity by the number of selected unique features (predictor + spatial statistic). Using the max validation RMSE yields different Pareto-optimal models, which are also evaluated. For models predicting Z , we convert predictions back to wind gust speed in physical units using the per-cluster GEV quantile function ($G_{\mu,\sigma,\xi}^{-1}$) before computing RMSE, which ensures consistency across model hierarchies.

4 Results

4.1 Pareto-Optimal Models for Wind Gust Prediction

We explore the (complexity, error) space of trained MLRs by varying hyperparameters—feature smoothing, retained variance, and target transformation—as well as the cross-validation strategy (mean or max validation RMSE). This allows us to identify Pareto-optimal maximum wind gust equations in low sample size conditions, forming the empirical *Pareto front* (dashed black line, Fig. 2b). When features are selected by minimizing the max validation RMSE, the minimum achievable RMSE stabilizes after 5 selected unique variables, suggesting that additional variables may not improve generalization to unseen cases. The steady decline in validation RMSE beyond 5 features sets an upper complexity limit, beyond which models lose their ability to generalize across regions and storms with different gust spatial patterns. Additionally, the Pareto front (Fig. 2b) indicates that models perform best when retaining 90% of PC variance and applying moderate smoothing (removing oscillations with frequency > 1.5 rad/hr). These hyperparameters yield features most likely to generalize well across all storm cases.

As expected, the performance table for the best *sparse* models from different feature selection methods (Table 1) shows that models targeting the transformed gusts (Z) generally underperform models directly targeting U_{gust} on the validation set when RMSE is measured in U_{gust} units. Additionally, cross-validation using the ‘‘ICP split’’ yields no validation RMSE improvement over naive random splitting. However, generalizable equations must perform robustly on unseen storms. While the ‘‘ICP split’’ sacrifices some training and validation skill, it successfully identifies sparse equations that generalize well to extreme cases like Storm Lothar, as evidenced by its low test RMSE. In contrast, equations discovered using random splits consistently perform worse on test sets, suggesting implicit overfitting to validation sets by selecting variables optimized for specific gust spatial distributions. The smaller error spread of U_{gust} models confirms their tendency to select sparse equations suboptimal for unseen cases, regardless of hyperparameters. Thus, splitting storms by their wind gust spatial distribution for cross-validation (‘‘ICP split’’), transforming the target using extreme value theory, and leveraging this information for feature selection leads to more reliable models, revealing features that better anticipate unseen cases.

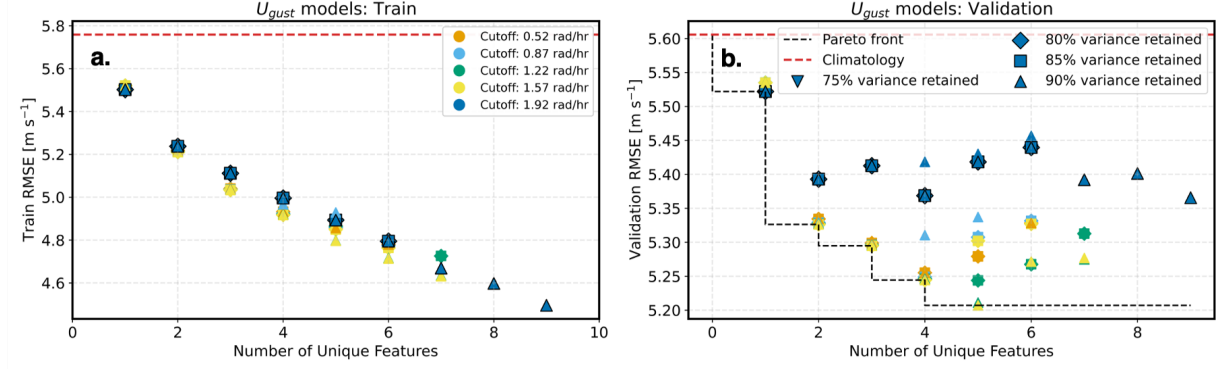


Figure 2: (a) Training and (b) validation (complexity, error) plots for MLR models predicting U_{gust} , with features selected to minimize the maximum validation RMSE across 7 randomly split cross-validation folds. Each colored symbol represents a model with different hyperparameters: cutoff frequency for smoothing is indicated by transparency levels, and retained feature variance by shape and color. The Pareto front (black dashed line in b) shows improved validation skills up to 5 unique features, suggesting that sparser linear models generalize better. In contrast, training RMSE decreases linearly with additional features, suggesting overfitting beyond 5 features. All models outperform the climatological baseline, which predicts the training mean U_{gust} and is shown as a red dashed line

Table 1: RMSE for the best models in the hierarchy, along with their unique feature count. We report the mean and the standard deviation (in parentheses) across feature selection methods and use bold font for the best RMSE. Model performance is compared to the climatology mean baseline to assess skill.

Feature selection methods	Feature count	Training	Validation	Test
Max RMSE; Random split; U	4	4.92 (0.06)	5.24 (0.30)	6.57 (0.02)
Mean RMSE; Random split; U	4	4.86 (0.13)	5.16 (0.75)	7.42 (0.01)
Max RMSE; Random split; Z	4	5.22 (0.09)	5.62 (0.42)	7.17 (0.02)
Mean RMSE; Random split; Z	4	5.04 (0.12)	5.39 (0.61)	7.17 (0.05)
Mean RMSE; ICP split; U	4	5.05 (0.14)	5.76 (1.14)	6.20 (0.01)
Max RMSE; ICP split; U	3	5.20 (0.13)	5.86 (0.93)	6.68 (0.01)
Mean RMSE; ICP split; Z	4	5.12 (0.14)	5.90 (1.15)	6.08 (0.03)
Max RMSE; ICP split; Z	3	5.40 (0.18)	6.00 (0.79)	6.47 (0.02)
Climatology; U; Random split	0	5.75	5.61	6.23
Climatology; U; ICP split	0	5.76	5.71	6.23

4.2 Reducing Geographical Bias through GEV-Informed Wind Gust Transformations

Why do the Z models outperform the U_{gust} models on the test set while underperforming on training and validation sets? To address this, we examine whether this performance gap varies across geographical regions. We compare the best U_{gust} and Z models trained with the “ICP split” feature selection method to assess regional differences in model skill. The U_{gust} model exhibits a distinct west-east RMSE gradient (Fig. 3a), with higher errors in Northwestern Europe, where severe windstorms frequently make landfall. This suggests that the model prioritizes inland clusters with weaker winds, potentially at the expense of distinguishing differences in strong coastal gusts (Fig. 3a). It may also struggle to anticipate rare inland windstorms, such as Storm *Aila* (2020) [Rantanen et al., 2021]. Therefore, the main difference between the U_{gust} and Z error maps (Fig. 3) is that the nonlinear gust transformation imposes stronger spatial regularization. The Z model shows decreased skill in Eastern Europe and the Balkans but improved performance in Northwestern Europe, suggesting reduced geographical bias. These results indicate that the GEV-informed gust transformation mitigates regional biases in MLR predictions, leading to a fairer model despite its slightly higher overall RMSE compared to U_{gust} MLRs.

4.3 Leveraging Interpretable, Pareto-Optimal Equations for Scientific Insight

Both the best 4-feature U_{gust} and Z models are linear functions of the *standardized* PC loadings, defined as $\widetilde{\text{PC}}_{X,j} = \frac{\text{PC}_{X,j} - \text{PC}_{X,j}^{\text{mean}}}{\text{PC}_{X,j}^{\text{std}}}$, where the mean and standard deviation are calculated over the training set and j indexes the selected features. After fitting, these standardized PC loadings are multiplied by region-specific weights $a_X \in \mathbb{R}^{15 \times 4}$ and then

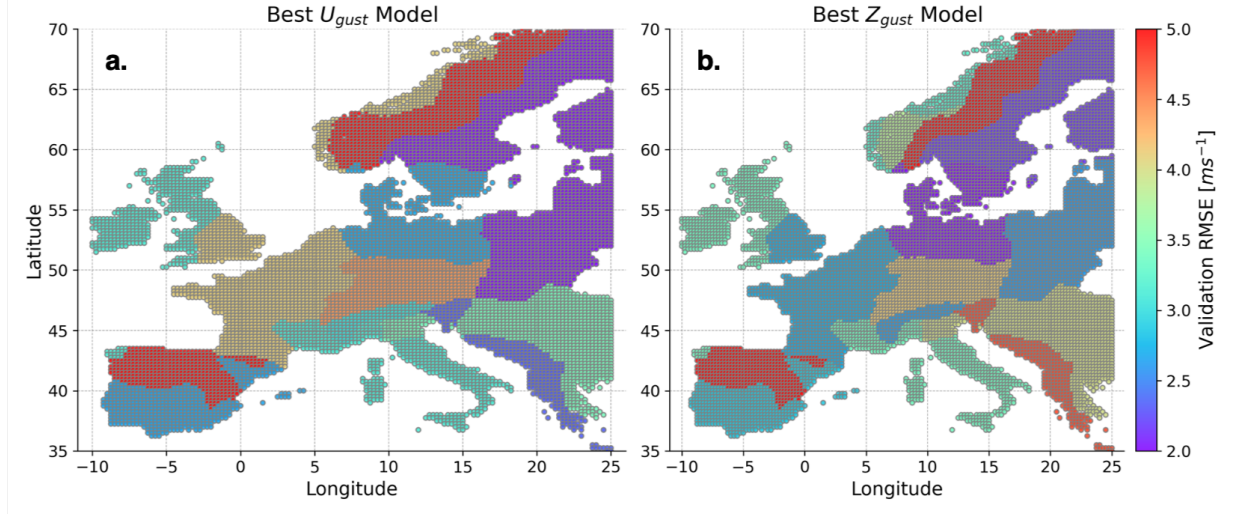


Figure 3: Validation error maps for (a) the best U_{gust} model and (b) the best Z model in physical units (m s^{-1}). The nonlinear, GEV-informed transformation reduces the west-east error gradient in U_{gust} and improves gust predictions in windstorm-prone Northwestern Europe

added to biases $\mathbf{b} \in \mathbb{R}^{15}$ for each of the 15 regions of interest. Using the inner product from Eq. 1, we express the models as scaled projections of winterstorm fields onto data-driven temporal patterns $\Pi_{X,j}(t)$. The equation for the U_{gust} model is:

$$U_{\text{gust}}^U = \beta^U + \sum_{j=1}^4 \alpha_{X,j}^U \langle \Pi_{X,j}(t) | X_j(t) \rangle_{X_j} \quad \text{where: } \alpha_{X,j}^U = \frac{a_{X,j}^U}{\overline{PC}_{X,j}^{\text{std}}}, \quad \beta^U = b^U - \sum_{j=1}^4 \frac{\overline{PC}_{X,j}^{\text{mean}}}{\overline{PC}_{X,j}^{\text{std}}} \mathbf{1}. \quad (3)$$

For the Z model, using the definition of Z and the GEV quantile function from Eq. 2, we obtain:

$$U_{\text{gust}}^Z = G_{\mu,\sigma,\xi}^{-1} \left(1 - \exp \left[-\beta^Z - \sum_{j=1}^4 \alpha_{X,j}^Z \langle \Pi_{X,j}(t) | X_j(t) \rangle_{X_j} \right] \right) \quad \text{with } (\alpha_{X,j}^Z, \beta^Z) \text{ similarly defined.} \quad (4)$$

U_{gust}^U and U_{gust}^Z are the predicted maximum wind gusts for each region using the direct and transformed models, respectively; $b^U, b^Z \in \mathbb{R}^{15}$ are region-specific biases; $a_{X,j}^U, a_{X,j}^Z \in \mathbb{R}^{15}$ are region-specific regression weights for the selected PC loadings; $\Pi_{X,j}(t)$ are the data-driven temporal patterns associated with each winterstorm feature; $\langle \Pi_{X,j}(t) | X_j(t) \rangle_{X_j}$ represents the projection of the storm field $X_j(t)$ onto the temporal mode $\Pi_{X,j}(t)$; $G_{\mu,\sigma,\xi}^{-1}$ is the GEV quantile function, mapping transformed values back to physical wind gust units; and $\mathbf{1} \in \mathbb{R}^{15}$ is the identity vector (a column vector of ones).

For a region i and a feature j , models predict higher $U_{\text{gust},i}$ when the product of $a_{X,j,i}$ and $\overline{PC}_{X,j}$ is positive, and vice versa. Assuming $a_{X,j,i} > 0$, time series that project positively onto the PC eigenvectors lead to higher wind gust predictions. The regression coefficients $a_{X,i}$ in the best Z model exhibit significant geographical variability (Fig. 4a-d), indicating that the influence of temporal patterns on gusts varies across regions. For example, two low-tropospheric humidity PCs in the Z model are positively correlated with gusts in region 4 (France and the Netherlands; Fig. 4a-b), while the other two PC terms are negatively correlated (Fig. 4c-d). The temporal evolution of the first PC mode of RH_{\max}^{850} and the third PC mode of RH_{\max}^{975} (Fig. 4e) suggests that higher gusts in France occur when drying persists within or at the top of the boundary layer (850 hPa) before storm landfall. A drier lower troposphere promotes the descent of high-speed winds via evaporation [Browning et al., 2015] or through downward mixing [Pantillon et al., 2018]. In contrast, a larger standard deviation of 500 hPa geopotential height (Φ) before landfall (Fig. 4f) may indicate more perturbed west-east winds, which can intensify winterstorms. To summarize, Fig. 4 demonstrates that we can extract important storm predictors leading to extreme wind gusts, such as low-tropospheric humidity, and quantify their relative importance. Finally, the temporal variability encoded in the PCs reveals additional insights into the timing of the drying or moistening tendency relative to landfall, which increases the likelihood of strong gusts.

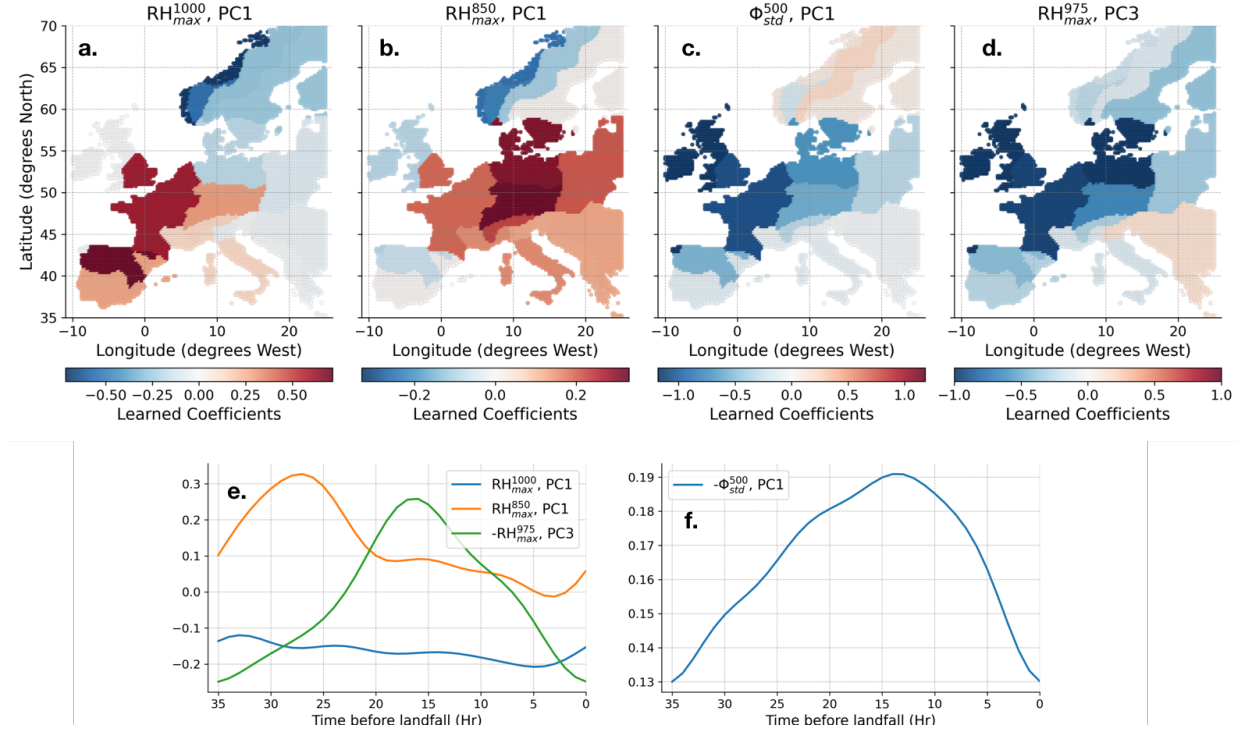


Figure 4: A visual representation of the learned weights for the 4 features in equation of our best Z model: (a) RH_{\max}^{1000} , (b) RH_{\max}^{850} , (c) RH_{\max}^{975} , and (d) Φ_{std}^{500} . Comparing these weights across clusters to the time series of the four selected PC modes (e-f) highlights key temporal patterns in storm history that promote or suppress extreme winds after landfall in different regions

5 Conclusion

We derived interpretable equations linking storm history to post-landfall extreme wind gusts through a PC-regression-based framework. By combining dimensionality reduction and temporal smoothing, we trained a hierarchy of equations from small datasets while mitigating overfitting via careful cross-validation, sequential feature selection, and Pareto optimization. Our results suggest that hierarchical modeling improves generalizability in small-sample settings, with the “Invariant Causal Prediction split” providing the greatest benefit for unseen test cases. Pareto optimization indicates that equations should contain at most 3–4 features to balance generalizability and predictive skill. While the best-performing U_{gust} model performs well globally (mean validation RMSE), spatial analysis reveals a west-east error structure, as the model prioritizes weak-wind regions at the expense of capturing gust variations in strong-wind regions. A GEV-informed nonlinear transformation reduces this spatial bias by accentuating distinctions in gust percentiles at the distribution tail. The discovered equations provide insights into how the timing of low-tropospheric drying is associated with wind gusts in Northwestern Europe, underscoring the importance of storm thermodynamic history in predicting post-landfall wind gusts. Future extensions could apply this framework to larger datasets and explore alternative interpretable modeling approaches, including nonlinear methods such as symbolic regression.

References

- David Arthur and Sergei Vassilvitskii. k-means++: The advantages of careful seeding. Technical report, Stanford, 2006.
- KA Browning, DJ Smart, MR Clark, and Anthony J Illingworth. The role of evaporating showers in the transfer of sting-jet momentum to the surface. *Quarterly Journal of the Royal Meteorological Society*, 141(693):2956–2971, 2015.
- Steven L Brunton, Joshua L Proctor, and J Nathan Kutz. Discovering governing equations from data by sparse identification of nonlinear dynamical systems. *Proceedings of the national academy of sciences*, 113(15):3932–3937, 2016.

- Gloria Buriticá and Sebastian Engelke. Progression: an extrapolation principle for regression. *arXiv preprint arXiv:2410.23246*, 2024.
- Shijun Cheng and Tariq Alkhalifah. Discovery of physically interpretable wave equations. *Surveys in Geophysics*, pages 1–26, 2024.
- Copernicus Climate Change Service, Climate Data Store. Winter windstorm indicators for europe from 1979 to 2021 derived from reanalysis. *Copernicus Climate Change Service (C3S) Climate Data Store (CDS)*, 2022. Accessed via Climate Data Store.
- Gregory G Enas and Sung C Choi. Choice of the smoothing parameter and efficiency of k-nearest neighbor classification. In *Statistical methods of discrimination and classification*, pages 235–244. Elsevier, 1986.
- A. Grundner, T. Beucler, P. Gentile, and V. Eyring. Data-driven equation discovery of a cloud cover parameterization. *Journal of Advances in Modeling Earth Systems*, 16(3):e2023MS003763, 2024. doi: 10.1029/2023MS003763.
- K. A. Hilburn. Understanding spatial context in convolutional neural networks using explainable methods: Application to interpretable gremlin. *Artificial Intelligence for the Earth Systems*, 2:220093, 2023.
- D. Häfner, J. Gemmrich, and M. Jochum. Machine-guided discovery of a real-world rogue wave model. *Proceedings of the National Academy of Sciences*, 120(48):e2306275120, 2023. doi: 10.1073/pnas.2306275120. URL <https://doi.org/10.1073/pnas.2306275120>.
- Y. Jin and B. Sendhoff. Pareto-based multiobjective machine learning: An overview and case studies. *IEEE Transactions on Systems, Man, and Cybernetics, Part C (Applications and Reviews)*, 38(3):397–415, 2008.
- Kirsti Jylhä, Heikki Tuomenvirta, Kimmo Ruosteenoja, Hanna Niemi-Hugaerts, Krista Keisu, and Juha A Karhu. Observed and projected future shifts of climatic zones in europe and their use to visualize climate change information. *Weather, Climate, and Society*, 2(2):148–167, 2010.
- R. Lagerquist, J. T. Allen, and A. McGovern. Climatology and variability of warm and cold fronts over north america from 1979 to 2018. *Journal of Climate*, 33:6531–6554, 2022.
- T. K. Laurila, H. Gregow, J. Cornér, and V. A. Sinclair. Characteristics of extratropical cyclones and precursors to windstorms in northern europe. *Weather and Climate Dynamics*, 2(4):1111–1130, 2021.
- A. Mamalakis, E. A. Barnes, and I. Ebert-Uphoff. Carefully choose the baseline: Lessons learned from applying xai attribution methods for regression tasks in geoscience. *Artificial Intelligence for the Earth Systems*, 2:e220058, 2023. doi: 10.1175/AIES-D-22-0058.1. URL <https://doi.org/10.1175/AIES-D-22-0058.1>.
- O. Martínez-Alvarado, S. L. Gray, P. A. Clark, and L. H. Baker. Objective detection of sting jets in low-resolution datasets. *Meteorological Applications*, 20(1):41–55, 2013.
- F. J. Méndez, M. Menéndez, A. Luceño, and I. J. Losada. Analyzing monthly extreme sea levels with a time-dependent gev model. *Journal of Atmospheric and Oceanic Technology*, 24:894–911, 2007.
- F. Pantillon, S. Lerch, P. Knippertz, and U. Corsmeier. Forecasting wind gusts in winter storms using a calibrated convection-permitting ensemble. *Quarterly Journal of the Royal Meteorological Society*, 144(715):1864–1881, 2018.
- F. Pedregosa, G. Varoquaux, A. Gramfort, V. Michel, B. Thirion, O. Grisel, M. Blondel, P. Prettenhofer, R. Weiss, V. Dubourg, J. Vanderplas, A. Passos, D. Cournapeau, M. Brucher, M. Perrot, and É. Duchesnay. Scikit-learn: Machine learning in python. *Journal of Machine Learning Research*, 12:2825–2830, 2011.
- J. Peters, P. Bühlmann, and N. Meinshausen. Causal inference by using invariant prediction: Identification and confidence intervals. *Journal of the Royal Statistical Society: Series B (Statistical Methodology)*, 78(5):947–1012, 2016. doi: 10.1111/rssb.12167. URL <https://doi.org/10.1111/rssb.12167>.
- M. Rantanen, T. K. Laurila, V. Sinclair, and H. Gregow. Storm aila: An unusually strong autumn storm in finland. *Weather*, 76(9):306–312, 2021.
- M. Schmidt and H. Lipson. Distilling free-form natural laws from experimental data. *Science*, 324(5923):81–85, 2009.
- B. Schulz and S. Lerch. Machine learning methods for postprocessing ensemble forecasts of wind gusts: A systematic comparison. *Monthly Weather Review*, 150:235–257, 2022.
- C. Schwierz, P. Köllner-Heck, E. Zenklusen Mutter, D. N. Bresch, P. L. Vidale, M. Wild, and C. Schär. Modelling european winter wind storm losses in current and future climate. *Climatic Change*, 101:485–514, 2010.
- W. Song, S. Jiang, G. Camps-Valls, M. Williams, L. Zhang, M. Reichstein, H. Vereecken, L. He, X. Hu, and L. Shi. Towards data-driven discovery of governing equations in geosciences. *Communications Earth & Environment*, 5(1): 589, 2024.
- L. Sweet, C. Müller, M. Anand, and J. Zscheischler. Cross-validation strategy impacts the performance and interpretation of machine learning models. *Artificial Intelligence for the Earth Systems*, 2:e230026, 2023.

- F. I.-H. Tam, T. Beucler, and J. H. Ruppert Jr. Identifying three-dimensional radiative patterns associated with early tropical cyclone intensification. *Journal of Advances in Modeling Earth Systems*, 16(12):e2024MS004401, 2024.
- H. Wernli, S. Dirren, M. A. Liniger, and M. Zillig. Dynamical aspects of the life cycle of the winter storm ‘lothar’ (24–26 december 1999). *Quarterly Journal of the Royal Meteorological Society*, 128:405–429, 2002.
- X. L. Xie and G. Beni. A validity measure for fuzzy clustering. *IEEE Transactions on Pattern Analysis and Machine Intelligence*, 13(8):841–847, 1991.

SUPPLEMENTARY MATERIAL: FROM WINTER STORM THERMODYNAMICS TO WIND GUST EXTREMES: DISCOVERING INTERPRETABLE EQUATIONS FROM DATA

Frederick Iat-Hin Tam

Faculty of Geosciences and Environment
University of Lausanne
Lausanne, VD, Switzerland

Fabien Augsburger

Faculty of Geosciences and Environment
University of Lausanne
Lausanne, VD, Switzerland

Tom Beucler

Faculty of Geosciences and Environment
University of Lausanne
Lausanne, VD, Switzerland

April 11, 2025

1 Introduction

The document expanded upon several methodological details discussed in the main text. The first section (Section A) justifies the use of a manually-selected K number in the K-means++ clustering algorithm to separate different geographical regions. We will show that an optimal K of 4 is insufficient to separate different European regions. For example, all European mountain ranges like the Alps and the Pyrenees are categorized into one cluster using the optimal number of K. The second section (Section B) provides the fitted GEV coefficients for the geographical clusters and the statistical goodness-of-fit test results to ensure that the wind characteristics follow a GEV distribution. The third section (Section C) provides the mean characteristics of the storm cases used in the “ICP split” cross-validation method, which achieves the best generalizable equations in our case. The fourth section (Section D) describes the variables used in the best 4-feature U_{gust} and Z models and the learned coefficients of the Z equation. The final section (Section E) summarizes the physical variables used to generate the storm history information used in this work.

A. The optimal number of K clusters is insufficient in finding coherent subregions

The section justifies the manual selection of 15 clusters during output preprocessing. The optimal cluster number when using a K-means clustering algorithm can be determined with the Silhouette Score analysis. Applying the Silhouette Score to our dataset with gusts conditions, surface elevation, longitude, and latitude yields an optimal K between 4 and 5 (Fig. 1). However, the optimal number of K=5 is insufficient to find coherent geographical clusters when all mountain ranges in Europe are classified as the same cluster, which is too wide for accurate assessment of the gust risk for synoptic-scale extratropical cyclones (Fig. 2). The other metrics in Figure 3 do suggest higher optimal cluster numbers. The Davies-Bouldin score suggests cluster numbers higher than 7, with 9 being the optimal number suggested by this metric. While the Xie-Beni score optimizes at a low cluster number of 4, it does have a local minima at 15 clusters. Finally, the Dunn score has a local maxima at the cluster number of 14.

Summarizing these results, we have 3 additional cluster number candidates in addition to the 4 clusters that we rejected on the basis of overly large clusters. These candidates are 9, 14, and 15. Figure 4 shows the unsmoothed version of the cluster maps with 9 and 14 clusters. Compared to our final cluster map, both options do not achieve the right geographical coherence and regional specificity for our purpose, particularly in southern Europe and the Balkans. Both

of these cluster maps consider a large part of Italy and the Carpathian Basin to be a single coherent entity. This is problematic as it is too large and violates established European climate regimes.

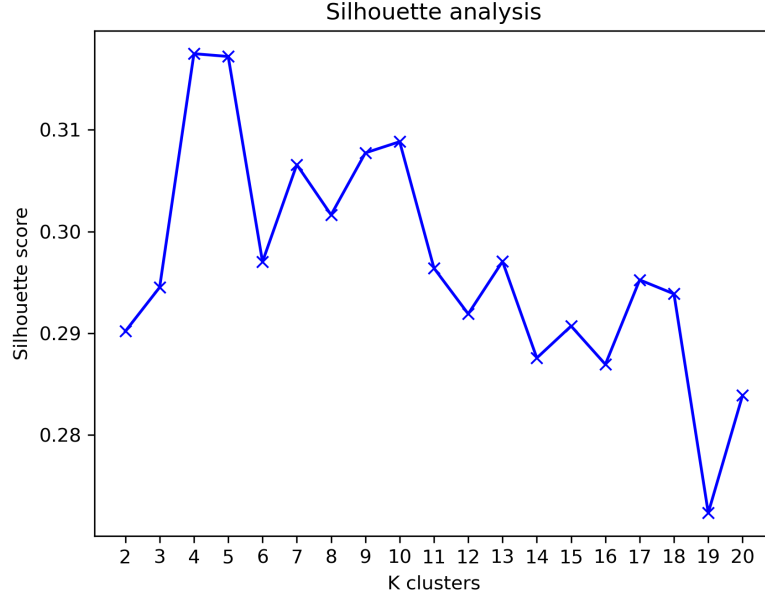


Figure 1: Silhouette analysis of the optimal K number to find coherent geographical subregions

B. GEV distributions

Fitted GEV coefficients for the geographical clusters

We provide a list of all fitted GEV coefficients for the 15 geographical clusters for preparing the nonlinear transformed Z_{gust} and Figure 1 in the main text.

Cluster number	Location	Scale	Shape
1	0.073	16.247	4.020
2	0.033	14.911	4.533
3	0.032	16.805	4.429
4	0.135	18.439	4.398
5	0.094	15.623	3.549
6	0.138	17.691	4.486
7	0.103	21.075	5.003
8	-0.023	13.722	4.563
9	0.132	17.204	3.982
10	0.137	16.468	4.272
11	0.047	16.844	3.795
12	0.120	16.232	5.364
13	0.102	19.381	4.827
14	0.128	17.504	4.564
15	0.112	15.716	4.879

Table 1: The fitted GEV coefficients of the 15 clusters

Statistical fitness tests to determine the definition of block maxima

To determine the definition of block maxima suitable for our data, we compare the empirical distribution to the fitted GEV distribution under different definitions of block maxima to test the goodness of fit. Using the p-value of

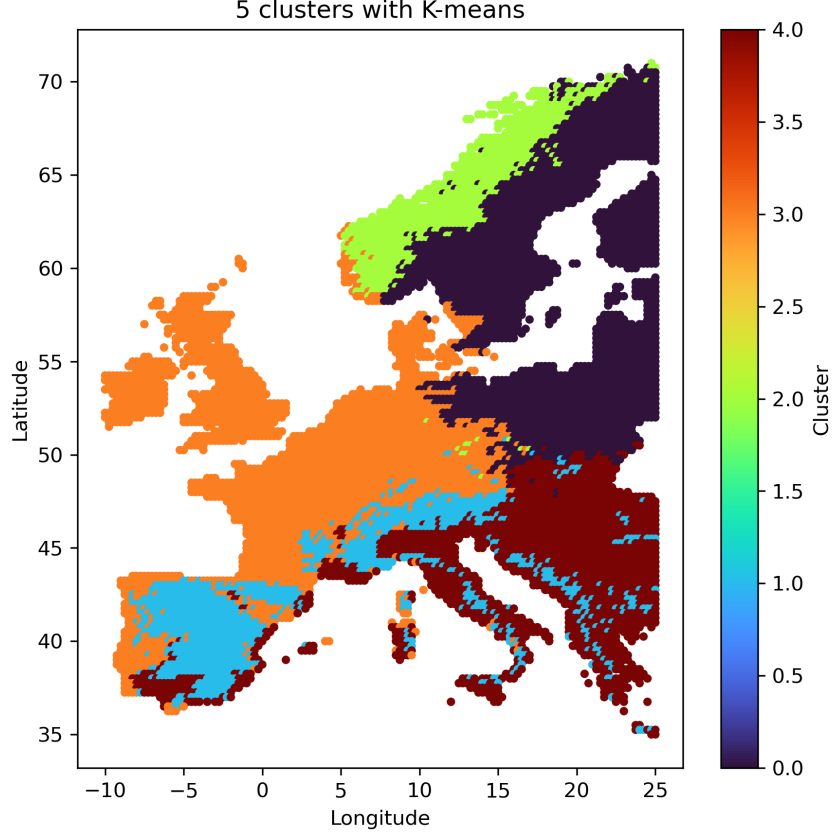


Figure 2: Classification of land grid points using the optimal number of K=5

Kolmogorov-Smirnov test, we see spatial variance in the GEV goodness-of-fits and a high sensitivity of the goodness-of-fit to block maxima definitions (Fig. 5). The overall best candidate for analysis was initially determined to be monthly maxima, as all clusters have p-values greater than the statistical threshold. However, we found that the maximum 15-hour wind speed for the storm events (maximum values) can occasionally fall outside the range of monthly maxima in some low winds regions as this definition removes too many low gust values. This ultimately lead to difficulties in getting to percentile values for all storms and clusters. With this in mind, we ultimately select daily maxima as our choice of block maxima in our study, with the caveat that the gusts in certain geographical regions (e.g., the Alps) cannot be accurately represented by the GEV fit.

C. Mean wind characteristics of the 7 Storm Case Clusters

The section shows the mean wind characteristics and the storm case counts of the seven storm case clusters used to produce the cross-validation folds based on storm gust characteristics. The mean gust winds of the storm clusters are shown, along with their corresponding storm counts (Table 2). From the table, we see a nice separation of windstorms with different spatial characteristics in their gust distribution. For example, the cluster with the lowest case count (Cluster 6) contains the two storms that had unusually high values in the 15th geographical cluster.

D. The sparse U_{gust} and Z_{gust} models

Selected variable list

This table describes the variables used in the best-performing sparse U_{gust} and Z_{gust} used to create Figure 3 in the main text. RH in the table represent relative humidity. The numerical information in the relative humidity terms represents the pressure levels of the selected relative humidity variable. The “max” in the variable list is the maximum value spatial

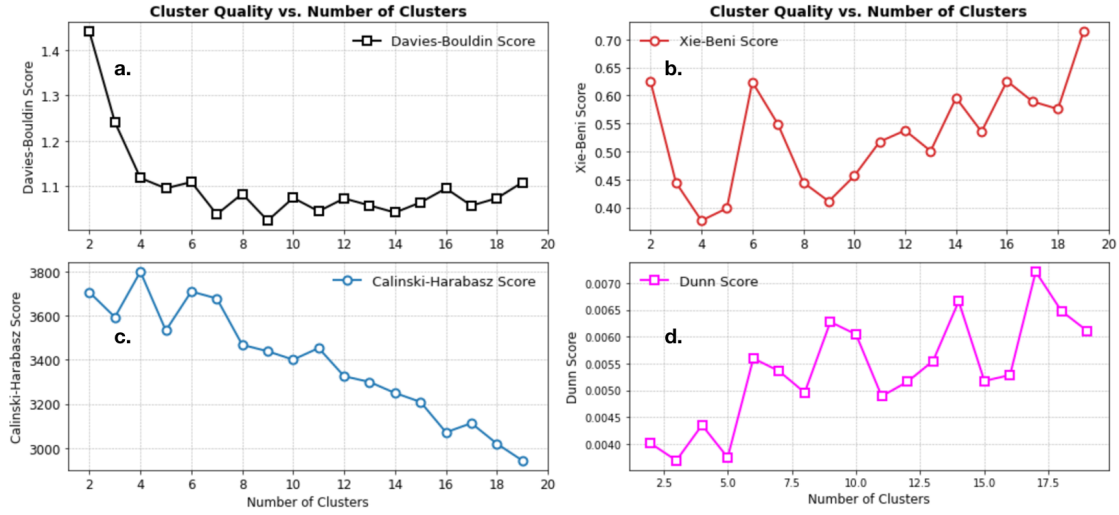


Figure 3: Cluster quality assessments with four different metrics. The upper row are metrics that suggests better cluster quality when the values are low, whereas the lower row shows metrics where higher values mean better cluster quality.

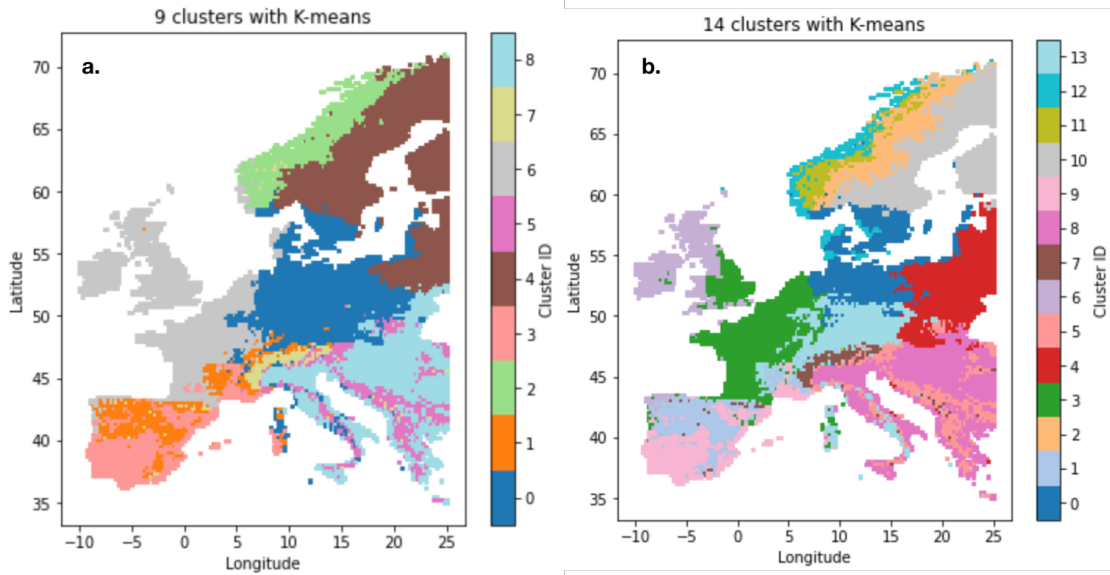


Figure 4: Raw, i.e., not smoothed with kNN algorithm, cluster maps with an optimal cluster number of (a) 9, and (b) 14.

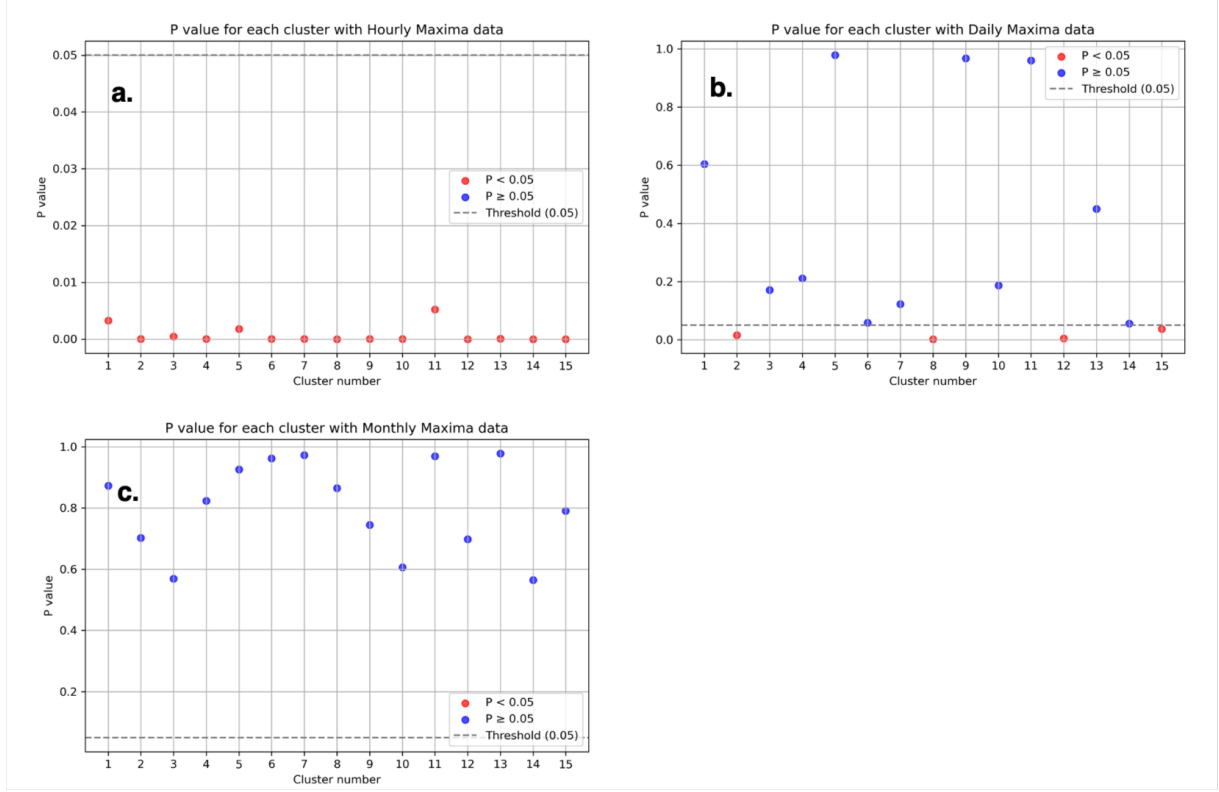


Figure 5: Statistical fitness test for different definitions of block maxima: hourly (a), daily (b), and monthly (c)

Cluster	Case Count	Mean Winds (m s^{-1})
1	15	25.39, 24.21, 16.32, 30.26, 18.49, 19.58, 37.57, 20.51, 17.75, 16.16, 17.87, 20.17, 20.08, 21.36, 18.90
2	11	18.65, 16.12, 17.84, 27.14, 14.86, 13.83, 39.46, 12.32, 14.54, 12.00, 17.59, 21.02, 22.05, 14.40, 18.25
3	6	31.74, 17.87, 29.68, 26.90, 23.59, 17.65, 42.15, 14.26, 16.04, 15.41, 26.47, 40.16, 41.85, 16.53, 13.94
4	8	17.54, 10.79, 27.21, 17.57, 15.86, 18.21, 31.36, 9.18, 18.10, 14.13, 23.38, 29.21, 33.70, 12.99, 12.88
5	10	30.58, 28.84, 21.19, 32.72, 23.49, 20.90, 42.69, 20.91, 20.53, 14.67, 21.56, 27.00, 26.86, 20.06, 17.74
6	2	18.55, 27.19, 17.95, 37.09, 18.52, 23.08, 37.49, 26.68, 17.48, 35.11, 18.88, 15.64, 18.14, 28.22, 43.35
7	4	19.96, 18.61, 23.05, 31.01, 15.72, 15.09, 34.93, 14.84, 15.90, 17.01, 20.41, 25.23, 26.87, 17.78, 28.75

Table 2: Mean wind speeds for different clusters

Order of selection	U_gust		Z_gust	
	Variable name	PC component	Variable name	PC component
1	RH_{max}^{1000}	1	RH_{max}^{1000}	1
2	RH_{max}^{850}	1	RH_{max}^{850}	1
3	$\overline{SW}_{net}^{TOA}_{std}$	3	Φ_{std}^{500}	1
4	$\overline{SW}_{net}^{surf}_{mean}$	3	RH_{max}^{975}	3

Table 3: Variables chosen by the best U_{gust} and Z_{gust} model

Cluster	RH_{max}^{1000}	RH_{max}^{850}	Φ_{std}^{500}	RH_{max}^{975}
1	-0.1853	0.3086	-0.7057	-1.1983
2	0.3043	0.3302	-0.5751	-0.6621
3	-0.2852	-0.1124	0.2235	-0.1178
4	0.6117	0.1952	-1.0632	-0.9501
5	-0.0888	0.2108	-0.3144	-0.3491
6	-0.0082	0.1228	-0.0277	0.1537
7	-0.0086	-0.0914	-1.1815	-1.2832
8	0.1560	0.2300	-0.3184	-0.3114
9	-0.0367	0.1280	-0.0438	0.1542
10	0.2830	0.0074	-0.1139	-0.2732
11	-0.2613	0.0100	0.0746	-0.3957
12	-0.5521	-0.2310	-0.2025	-0.2643
13	-0.7420	-0.2545	0.1037	-0.1978
14	0.1403	0.1564	-0.0766	-0.1255
15	0.7162	-0.0719	-0.5385	-0.4183

Table 4: The mean learned weights values of the best Z_{gust} model for the 15 clusters across the server splits.

filter, “mean” the mean value filter, and “std” the standard deviation filter. The \overline{SW}_{net} term in the table represents net shortwave radiation flux either at the top of the atmosphere (*TOA*) or at the surface (*surf*).

Learned coefficient for the best Z_{gust} model

Table 4 summarizes the learned coefficient of the best Z_{gust} model.

Normalization coefficients for the best Z_{gust} model

Here, we show the normalization coefficients used to standardize the PC time series for the four PC components in the best Z_{gust} model.

Variable	μ	σ
RH_{max}^{1000}	0.00031	0.05437
RH_{max}^{850}	-0.01020	0.10174
Φ_{std}^{500}	1.05e-17	2.77e-17
RH_{max}^{975}	0.00067	0.02530

Table 5: Normalization coefficients for the four variables in the best Z_{gust} model

E. Lists of environmental predictors in the dataset

The table describes the 28 environmental predictors used to build the storm history dataset. We categorize different predictors into kinematics, thermodynamics, and other predictors for reference.

Predictor	Category	Units
10m wind speeds	Kinematics	$m s^{-1}$
100m wind speeds	Kinematics	$m s^{-1}$
10m wind direction	Kinematics	degrees
100m wind direction	Kinematics	degrees
2m Temperature	Thermodynamics	K
2m Dewpoint Temperature	Thermodynamics	K
Mean surface net LW radiation flux	Thermodynamics	$W m^{-2}$
Mean surface net SW radiation flux	Thermodynamics	$W m^{-2}$
Mean surface latent heat flux	Thermodynamics	$W m^{-2}$
Surface latent heat flux	Thermodynamics	$J m^{-2}$
Mean surface sensible heat flux	Thermodynamics	$W m^{-2}$
Surface sensible heat flux	Thermodynamics	$J m^{-2}$
Mean TOA net LW radiation flux	Thermodynamics	$W m^{-2}$
Mean TOA net SW radiation flux	Thermodynamics	$W m^{-2}$
Relative Humidity	Thermodynamics	percent
Mean vertically-integrated moisture divergence	Thermodynamics	$mm s^{-1}$
Large-scale snowfall	Precipitation	m
Large-scale precipitation	Precipitation	m
Mean large-scale precipitation rate	Precipitation	$mm s^{-1}$
Mean total precipitation rate	Precipitation	$mm s^{-1}$
Total precipitation/1hour	Precipitation	m
Mean sea level pressure	Other	Pa
Surface pressure	Other	Pa
Convective Available Potential Energy	Thermodynamics	$J kg^{-1}$
Geopotential Height	Thermodynamics	$m^2 s^{-2}$
High Cloud Cover	Other	percent
K-index	Thermodynamics	K
Total totals index	Thermodynamics	K

Table 6: The 28 kinematic, thermodynamic, and other environmental predictors used to produce the input dataset